Volume 9 | Number 6 | 21 March 2022

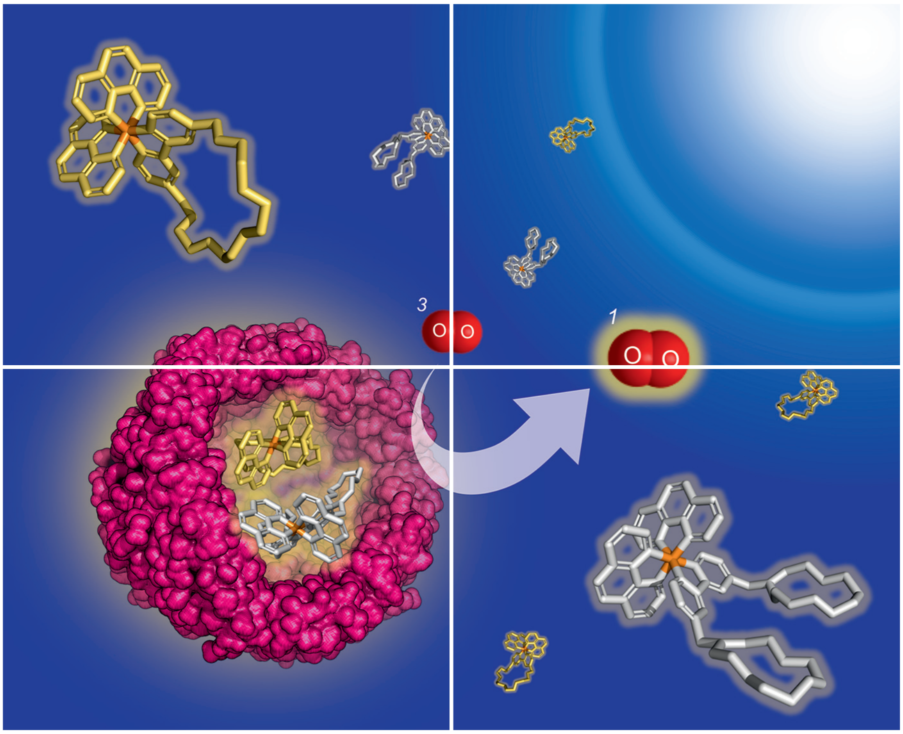

INORGANIC CHEMISTRY FRONTIERS

CCS 中国化学会 CHINESE CHEMICAL SOCIETY
PEKING UNIVERSITY 1898
ROYAL SOCIETY OF CHEMISTRY
rsc.li/frontiers-inorganic

INORGANIC CHEMISTRY
FRONTIERS

CHINESE CHEMICAL SOCIETY

ROYAL SOCIETY OF CHEMISTRY

RESEARCH ARTICLE

View Article Online
View Journal | View Issue

Cite this: *Inorg. Chem. Front.*, 2022, **9**, 1070

Ferritin nanocomposites for the selective delivery of photosensitizing ruthenium-polypyridyl compounds to cancer cells†

Luca Conti, *‡[a] Silvia Ciambellotti, *‡[b,c] Gina Elena Giacomazzo,[a] Veronica Ghini,[a,c] Lucrezia Cosottini,[a,c] Elisa Puliti,[d] Mirko Severi, [a] Emiliano Fratini, [a,e] Francesca Cencetti, [d] Paola Bruni,[d] Barbara Valtancoli,[a] Claudia Giorgi [a] and Paola Turano [a,b,c]

Received 7th October 2021,
Accepted 7th December 2021

DOI: 10.1039/d1qi01268a

rsc.li/frontiers-inorganic

Herein, we report on the successful encapsulation into human H-ferritin of two highly charged Ru(II) polypyridyl complexes, $[Ru(phen)_2\mathbf{L'}]^{2+}$ (**Ru1**, with **L′** = 4,4′-(2,5,8,11,14-pentaaza[15])-2,2′-bipyridilophane) and $[Ru(phen)_2\mathbf{L''}]^{2+}$ (**Ru2**, with **L″** = 4,4′-bis-[methylen-(1,4,7,10-tetraazacyclododecane)]-2,2′-bipyridine). The resulting Ru(II)-ferritin nanocomposites are highly luminescent, display great stability in physiological conditions and preserve the native shell–core structure of the protein. Moreover, the singlet oxygen sensitizing properties of metal complexes, established by independent spectrophotometric and spectrofluorimetric measurements, are largely maintained also in their encapsulated form. Ru(II)-ferritin nanocomposites are exclusively internalized by cancer cells expressing the transferrin receptor 1 (TfR1) (*i.e.* HeLa and A2780 with respect to non-cancerous C2C12 myoblasts). Immunofluorescence analysis also reveals the co-localization of **Ru1** and **Ru2** with the TfR1 in the internal cellular compartments of HeLa and A2780 cells, highlighting the crucial role played by the receptor-mediated endocytosis of H-type ferritins exerted by TfR1. Finally, an MTT assay probed that light-activation effectively leads to a marked dose-dependent cytotoxic effect uniquely against cancer cells. This study underlines the potential of human H-ferritin as a valuable tool for the tumor-targeted delivery of sensitizing agents for photodynamic therapy.

Introduction

Human ferritin is a heteropolymeric nanocage of 24 subunits involved in iron storage and release, depending on cellular demand.[1] Iron accumulates into ferritin under the form of a ferric-oxo biomineral that starts to grow from iron clusters on the inner surface of the protein cage following iron(II) oxidation by diffusing O_2.[2–7] While *in vivo* the heavy- and light-chains (H- and L-respectively) self-assemble at variable ratios to form the characteristic hollow structure with an internal cavity of 8 nm, recombinant ferritins are generally expressed as homopolymeric pure-H and pure-L cages. The potential of recombinant homopolymeric human H-ferritin (HuHf) as a valuable nanocarrier relies mainly on its low immunogenicity upon administration due to its human origin,[8] the possibility to incorporate low-molecular weight compounds[8] and the well-known interaction with transferrin receptor 1 (TfR1) for endocytosis.[9,10] In addition, the overexpression of TfR1 in cancer cells and the possibility of decorating the external surface with different targeting moieties make HuHf a promising platform for targeted drug delivery in cancer therapy.[11] Among the variety of possible biomedical applications,[12–17] ferritin may be a safe vehicle for small molecules designed for photodynamic therapy (PDT).[18–20]

PDT is based on the use of a photosensitizer (PS) that can be light-activated to produce reactive oxygen species (ROS), such as the highly cytotoxic singlet oxygen ($^1O_2$), and takes advantage of a complete spatial and temporal control over drug activation.[18] Thus, the use of ferritin-based nanocarriers in PDT opens the way to novel PS candidates with enhanced

---

[a] *Department of Chemistry "Ugo Schiff", University of Florence, Sesto Fiorentino 50019, Italy. E-mail: luca.conti@unifi.it*
[b] *Consorzio Interuniversitario Risonanze Magnetiche di Metallo Proteine (C.I.R.M.M.P.), Sesto Fiorentino 50019, Italy. E-mail: ciambellotti@cerm.unifi.it*
[c] *Magnetic Resonance Center (CERM), University of Florence, Sesto Fiorentino 50019, Italy*
[d] *Department of Experimental and Clinical Biomedical Sciences "Mario Serio", University of Florence, Florence 50134, Italy*
[e] *CSGI, University of Florence, Sesto Fiorentino 50019, Italy*

† Electronic supplementary information (ESI) available. See DOI: 10.1039/d1qi01268a

‡ These authors contributed equally.

selectivity and efficiency as has been found for a series of porphyrin derivatives, phthalocyanines and phenothiazine dyes.[21–25] In this scenario, Ru(II)-polypyridyl complexes are attracting PSs due to their high thermodynamic/kinetic stability, good singlet oxygen sensitizing capabilities and their vast photophysical and electrochemical repertoire, which can be tuned by a fine choice of ligands.[26–28]

Notwithstanding the enormous PDT potential, the employment of ferritin of human origin to modulate the drug delivery of Ru(II)-polypyridyl-based PSs remains an issue almost completely unexplored.[29] To date, only a few cases have been reported by Feng and coworkers,[30] with the encapsulation of the hydrophobic $[Ru(bpy)_3]^{2+}$, $[Ru(bpy)_2dppz]^{2+}$ and $[Ru(phen)_2dppz]^{2+}$ (bpy = bipyridine, phen = phenanthroline, dppz = dipyrido[3,2-*a*:2′,3′-*c*]phenazine) into horse spleen L-apoferritin. However, the $^1O_2$ sensitization by Ru(II)-ferritin systems was not evaluated.

We have previously reported on the potential of highly charged Ru(II)-polypyridyl complexes $[Ru(phen)_2\mathbf{L'}]^{2+}$ (**Ru1**) and $[Ru(phen)_2\mathbf{L''}]^{2+}$ (**Ru2**) as PS agents, featuring the peculiar polyazamacrocyclic units **L′** and **L″** (**L′** = 4,4′-(2,5,8,11,14-pentaaza[15])-2,2′-bipyridilophane, **L′** = 4,4′-bis-[methylen-(1,4,7,10-tetraazacyclododecane)]-2,2′ bipyridine).[31,32] The presence of many easily protonatable nitrogen groups on the unique polyazamacrocyclic moiety of **Ru1**, or on the two distinct cyclen (1,4,7,10-tetraazacyclododecane) units of **Ru2**, appended to the 4,4′ position of a metal-coordinated bipyridyl ligand affords the formation of highly charged species in aqueous media.[31,33] This confers to the resulting Ru(II) complexes not only excellent water solubility, a necessary prerequisite for their biological applications, but also strengthens their interaction with important biological targets, such as DNA. On the other hand, the polyamino-modified bipyridyl frameworks do not affect the good $^1O_2$ sensitizing capabilities of **Ru1** and **Ru2** ($\Phi_{\Delta(\mathbf{Ru1})} = 0.29 \pm 0.06$ and $\Phi_{\Delta(\mathbf{Ru2})} = 0.38 \pm 0.08$ in air-saturated CH_3CN, $\lambda = 400$ nm), thus making them attractive PS agents for the light-promoted $^1O_2$ generation directly in aqueous media.

Herein, we report on the encapsulation of **Ru1** and **Ru2** within HuHf to obtain the respective nanocomposites, **Ru1**@HuHf and **Ru2**@HuHf. The two hybrid systems underwent an extensive chemical–physical characterization, which included the analysis of their structural, luminescence and photosensitizing properties. The TfR1-mediated internalization and the biological potential of Ru(II)-HuHf nanocomposites were comparatively tested on representative cancer and non-cancer cell lines. The crucial role played by TfR1-mediated recognition of **Ru1**@HuHf and **Ru2**@HuHf in their selective delivery, and the different cytotoxic activities found against the tested cellular models, are also described.

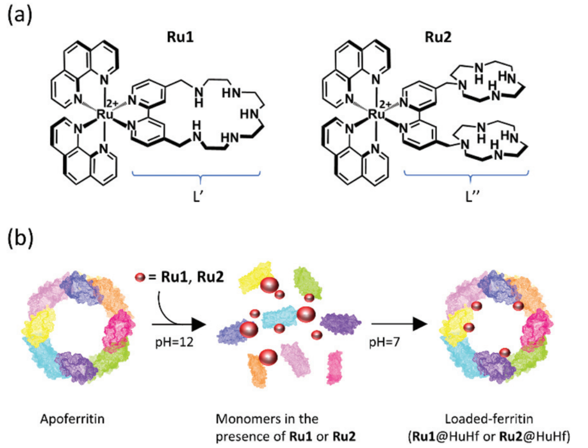

Fig. 1 (a) Ruthenium photosensitizers **Ru1** and **Ru2**; the respective macrocycle units **L′** and **L″** are indicated. (b) PSs encapsulation into HuHf by exploiting the pH-assisted disassembly/reassembly method.

Results and discussion

Encapsulation of Ru-polypyridyl complexes into ferritin

The large dimension of the **Ru1** and **Ru2** metal complexes (Fig. 1a) hampers their inclusion into HuHf by means of passive diffusion through the limited pore size (about 0.3 nm) of the protein shell.[8] For this reason, loading of **Ru1** and **Ru2** into HuHf was accomplished by the pH assisted disassembly and reassembly method harnessing the ability of ferritin to partially dissociate at pH 12 followed by the reconstitution of the 24-mer cage at neutral pH (Fig. 1b; see the ESI for more details, Fig. S3 and S4†).[8,34,35] As **Ru1** and **Ru2** are highly hydrophilic and stable even at pH 12,[31,33] they were incubated in the presence of HuHf during the disassembly process at different molar ratios (20–200 fold with respect to the protein). In order to remove the excess of **Ru1** or **Ru2**, *i.e.* the compounds not entrapped into the ferritin cavity, protein samples were purified by ultrafiltration and then subjected to size exclusion chromatography to recover the fraction corresponding to the fully reconstituted 24-mer cage containing **Ru1** and **Ru2** (**Ru1**@HuHf and **Ru2**@HuHf, respectively) (Fig. 2d).

Characterization of nanocomposites

The successful encapsulation of **Ru1** and **Ru2** was assessed by different means. A ligand to protein cage ratio of 5 and 4, for **Ru1**@HuHf and **Ru2**@HuHf respectively, was obtained as determined by UV-visible and ICP-AES analysis (Table 1). In this regard, only a few examples concerning the encapsulation of Ru(II) compounds into ferritin nanocages, accomplished by the pH assisted method, have been reported so far. Merlino and coworkers[37] encapsulated up to 36 molecules of $[(h^6\text{-}p\text{-}MeC_6H_4iPr)_2\mathbf{Ru_2}(m_2\text{-}S\text{-}p\text{-}C_6H_4tBu)_3]Cl$ per ferritin cage whereas the hydrophobic $[Ru(bpy)_3]^{2+}$, $[Ru(bpy)_2dppz]^{2+}$ and $[Ru(phen)_2dppz]^{2+}$ compounds reported by Feng *et al.*[30] were loaded in a ratio between 7–40 molecules per ferritin cage. However, all these studies referred to horse-spleen ferritin. ICP-AES measurements showed a negligible amount of ruthenium bound to the protein for the products obtained *via* direct incubation of Ru(II)-compounds in the presence of HuHf at pH 7 (without any disassembly process), thus confirming that the disassembly process is fundamental for **Ru1**/**Ru2** encapsula-

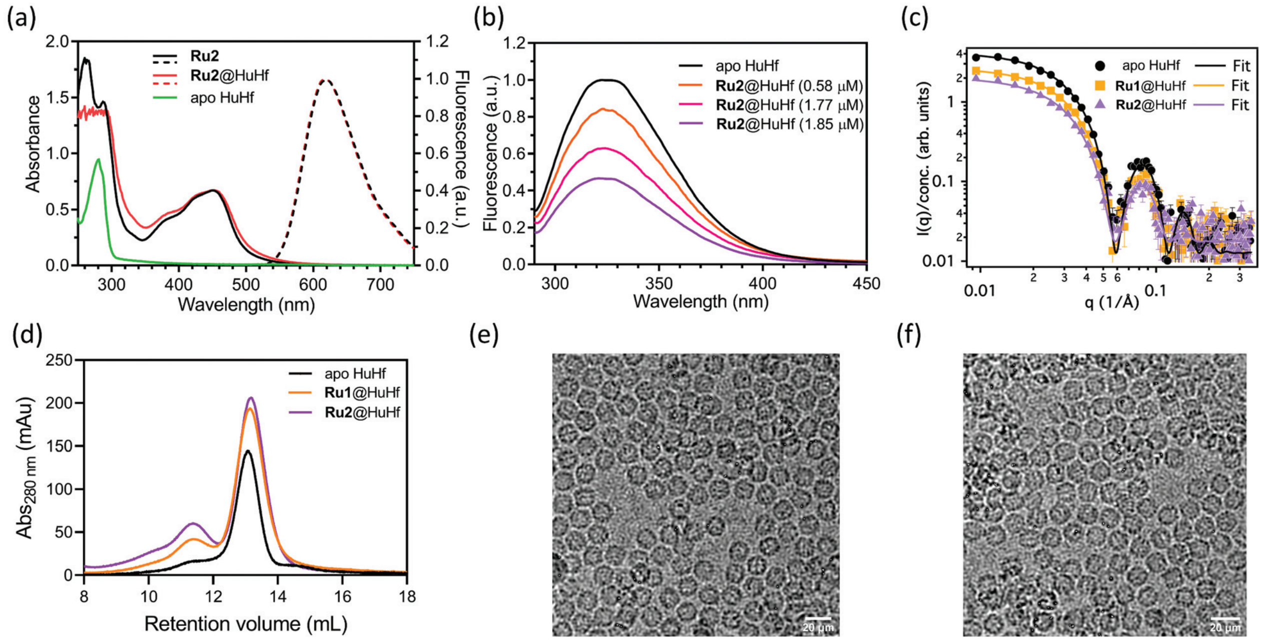

Fig. 2 Characterization of Ru(II)-HuHf nanocomposites. (a) Combined UV-visible and fluorescence spectra (λ_{exc} 411 nm) of free **Ru2** and of **Ru2**@HuHf (Ru(II) concentration of 50 μM and 6 μM for UV-visible and fluorescence measurements, respectively). UV-vis spectrum of apo HuHf is shown as reference. (b) Intrinsic fluorescence emission of apo HuHf and of **Ru2**@HuHf (HuHf 0.32 μM, λ_{exc} 280 nm) with increasing amounts of encapsulated **Ru2**. (c) SAXS intensity distribution of apo HuHf, **Ru1**@HuHf and **Ru2**@HuHf (markers represent experimental data while continuous lines refer to the core–shell modelling according to eqn (S1), ESI†). (d) Size exclusion chromatography analysis of ferritin nanocomposites upon encapsulation of **Ru1** and **Ru2** in 50 mM sodium phosphate pH 7 buffer. Chromatograms of encapsulated products were superimposed with the reference chromatogram of apo HuHf not subjected to the disassembly process. Eluted fractions related to peaks centered at about 13 mL of retention volume were taken for the subsequent experiments, thus corresponding to the reconstituted polymeric HuHf composed by 24 subunits. (e) and (f) Cryo-EM representative micrographs of **Ru1**@HuHf and **Ru2**@HuHf, respectively.

Table 1 Characterization of Ru(II)-loaded ferritin assemblies

	Ru atoms/cage					SAXS modeling[c]	
Sample name	UV vis-based	ICP AES-based	$\lambda_{Abs}/\lambda_{em}$ (nm)	k_{obs} [a] (min^{-1})	Φ_Δ [b]	Core diameter (nm)	Shell thickness (nm)
$[Ru(phen)_3]^{2+}$	—	—	447/605[d]	0.0595 (±5)	0.38 ± 0.08	—	—
Ru1	—	—	452/615	0.0434 (±3)	0.29 ± 0.06	—	—
Ru2	—	—	452/615	0.0594 (±4)	0.36 ± 0.08	—	—
Apo HuHf	—	—	—	—	—	8.32 ± 0.08	2.17 ± 0.06
Ru1@HuHf	5.2 ± 0.8[e]	4.1 ± 0.5[e]	452/615	0.0061 (±5)	—	8.14 ± 0.08	2.34 ± 0.09
Ru2@HuHf	4.3 ± 0.5[e]	3.4 ± 0.4[e]	452/615	0.0067 (±4)	—	8.02 ± 0.08	2.48 ± 0.10

[a] Photo-oxidation rate constants (k_{obs}) spectrometrically determined by the photo-oxidation of DHN in aqueous media at neutral pH. [b] Quantum yields (φ_Δ) of singlet oxygen production determined by measurements of $^1O_2$ phosphorescence at 1270 nm in air saturated CH_3CN solutions. [c] Parameters obtained using a core–shell model (see eqn (S1) in the ESI).† [d] Values determined in water at 298 K.[36] [e] Mean values with SEM of three independent experiments.

tion. The slight differences in the overall positive charge on compounds $[H_2\mathbf{Ru1}]^{4+}$ and $[H_4\mathbf{Ru2}]^{6+}$ at physiological pH only marginally affect the PS-loading content. The structural integrity of the nanocomposites was evaluated by single particle cryo-TEM micrographs acquired on **Ru1**@HuHf and **Ru2**@HuHf (Fig. 2e and f) showing the maintenance of the spherical nanocage structure characteristic of the apo HuHf, with an external diameter of 12 nm (ESI, Fig. S2 and S9†). CD spectra of apo HuHf, (**Ru1**/**Ru2**)@HuHf were acquired in the far UV region to control their stability looking at the signal intensities belonging to α-helix, which is the preeminent secondary structure element of ferritin. The results showed that the extraordinary structural stability of ferritin is preserved even after pH-guided encapsulation as observed in the temperature range of 25–85 °C (ESI, Fig. S8†).

The absorbance and fluorescence profiles of **Ru1**@HuHf and **Ru2**@HuHf were then analyzed. As shown in Fig. 2a and Fig. S5a (ESI),† the absorbance spectra of **Ru1**@HuHf and **Ru2**@HuHf are almost identical to the reference spectra of the free ligands; the typical MLCT band of ruthenium complexes within the 400–500 nm range, well separated from the apoferritin background, indicates that no ligand-exchange occurred during the encapsulation process. (**Ru1**/**Ru2**)@HuHf nanocomposites feature marked fluorescence properties. In fact, **Ru1** and **Ru2** retain their native emission upon internalization into the protein (λ_{exc} 411 nm, λ_{em} 615 nm; Fig. 2a and ESI, Fig. S5a†). In addition, the intrinsic fluorescence emission of ferritin, generated from its tryptophan and tyrosine moieties (λ_{exc} 280 nm, λ_{em} 325 nm; ESI, Fig. S6†), was registered. A progressive quenching of the intrinsic fluorescence of the protein with increasing amounts of internalized ruthenium species evidenced the interaction between metal complexes and the protein, as shown for **Ru2**@HuHf and **Ru1**@HuHf in Fig. 2b and the ESI, Fig. S5b,† respectively and as reported for similar systems.[38,39] The interaction of the compounds with ferritin was further explored by ^{1}H NMR spectroscopy. CPMG experiments, which are designed to selectively observe the signals from low molecular weight compounds in mixtures containing large biomolecules by removing the broad unwanted resonances of the latter,[40,41] were performed. The ^{1}H NMR signals corresponding to **Ru1** and **Ru2** in the encapsulated formulations are broad beyond detection, most likely due to the interaction with the protein (ESI, Fig. S7a and b†). In contrast, if the same amount of Ru-compound is added to a solution of HuHf at neutral pH, the resonances belonging to the ligand are visible in the spectrum with line widths comparable to those of the individual metal compounds. These observations suggest that (**Ru1**/**Ru2**)@HuHf nanocomposites contain Ru complexes encapsulated inside the cage and that these complexes do not freely rotate inside the cavity but rather interact with the inner cage surface (ESI, Fig. S7a and b†). The SAXS patterns for the apo HuHf before and after Ru(II) complex internalization further show that the hollow shell structure of the protein is retained (Fig. 2c). In all cases, extracted density profiles are in agreement with a core–shell form factor characterized by the electron density of the core (cavity) being equal to that of the buffer solution (*i.e.* hollow shell system). The overall size of the cavity slightly decreases with the insertion of the Ru(II) complexes from 8.32 nm in the case of the apo form to 8.13 nm and 8.02 nm for **Ru1**@HuHf and **Ru2**@HuHf, respectively (Table 1). This shrinkage is directly associated with the increase of the thickness of the protein shell from about 2.2 nm to 2.5 nm and a good fit of these data could only be achieved considering the hollow shell topology. The increment in shell thickness and the simultaneous reduction in the diameter of the cavity confirmed that **Ru1** and **Ru2** are likely localized in proximity to the internal protein surface. Taken together, SAXS and NMR data lead us to hypothesize that the interaction of **Ru1** and **Ru2** with HuHf would be driven by electrostatic contributions between the metal compounds ($[H_2\mathbf{Ru1}]^{4+}$ and $[H_4\mathbf{Ru2}]^{6+}$), namely through the positively charged polyammonium groups on their **L′** and **L″** units, and the negatively charged residues facing the inner cavity of the protein.[42] On the other hand, an additional evidence that the interaction of the Ru compounds with the protein does not occur on the external surface arose by the comparison of zeta potential measurements of Ru-nanocomposites with respect to apo HuHf. The zeta potentials resulted to be similar under the experimental error, that are, − 5.0 ± 1.1 mV and − 3.1 ± 0.4 mV for **Ru1**@HuHf and **Ru2**@HuHf, respectively and − 4.2 ± 0.6 mV for apo ferritin, ruling out any external interaction of **Ru1** and **Ru2** with the protein.

Singlet oxygen production from ruthenium-ferritin assemblies

The capacity of Ru(II)-ferritin nanocomposites to generate singlet oxygen upon light-activation was assessed by employing two indirect chemical trapping methods (*vide infra*) and using water-soluble substrates as scavengers for $^1O_2$ (Fig. 3a and b). The results were then compared with those obtained for the 'non encapsulated'-PSs and for $[Ru(phen)_3]^{2+}$, the latter taken as reference for $^1O_2$ generation (Φ_Δ = 0.21 in air equilibrated D_2O).[43] Firstly, 1,5-dihydroxynaphthalene (DHN) was used as an indirect singlet oxygen reporter exploiting its prompt and quantitative oxidation in the presence of $^1O_2$ to give 5-hydroxy-1,4-naphthalenedione (Juglone), according to eqn (S2) and Scheme S1 (ESI).† This process can be easily followed *via* UV-vis spectroscopy by monitoring the decrease of the DHN absorption band at λ_{max} 297 nm and the simultaneous increase of the broad Juglone band centered at *ca.* 427 nm.[44,45]

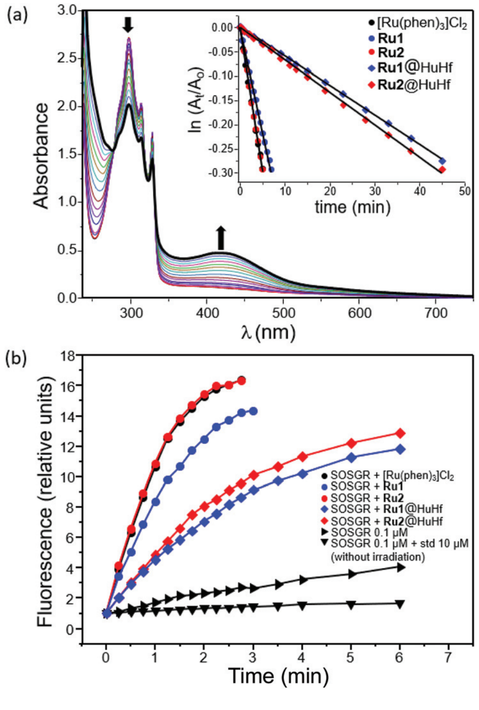

Fig. 3 (a) Absorption spectra of an aqueous solution at pH 7 containing DHN and **Ru2**@HuHf at different irradiation times (up to 7 minutes). As blank reference we used a solution containing the PS at the same concentration and pH of that of the measuring cuvette. In the inset the semilogarithmic plots of $\ln(A_t/A_0)$ as a function of the irradiation time obtained for all the investigated systems ([DHN] = 3.3×10^{-4} M, [Ru] = 10 μM, 50 mM NaPi buffer) are compared. (b) Singlet oxygen production from free and HuHf-loaded Ru(II) PSs as monitored by the Singlet Oxygen Sensor Green reagent (SOSGR) in 50 mM NaPi buffer, (pH 7), ([SOSGR] = 0.5 μM, [Ru] = 5 μM, $\lambda_{exc}/\lambda_{em}$ 488/525 nm).

Experiments were carried out by irradiating (LED light, $\lambda >$ 430 nm, 30 W) aqueous solutions, pre-saturated with O_2, and containing sensitizers (**Ru1**, **Ru2**, **Ru1**@HuHf, **Ru2**@HuHf or $[Ru(phen)_3]^{2+}$) in the presence of DHN. Negligible Juglone formation was observed upon DHN irradiation in the absence of sensitizers under these experimental conditions (ESI, Fig. S11a†). As shown in Fig. S11e (ESI)† and Fig. 3a, which respectively report the UV-vis titrations obtained for **Ru1**@HuHf and for **Ru2**@HuHf (those obtained for the non-encapsulated PSs are shown in the ESI, Fig. S11b–d†), light-activation of Ru-ferritin nanocomposites determines the progressive decrease of the DHN absorption band, along with the simultaneous increase of the Juglone band, clearly demonstrating the capacity of Ru(II)-ferritin nanocomposites to efficiently sensitize $^1O_2$ production. Moreover, the appearance in these spectra of two clear isosbestic points around 280 and 330 nm ruled out the formation of long-lived intermediates or byproducts. In particular, as better shown by the inset in Fig. 3a, which reports the semilogarithmic plots of $\ln(A_t/A_0)$ obtained for all the Ru(II)-based formulations over the investigated irradiation time frame, Ru(II)-ferritin nanocomposites produce a similar amount of $^1O_2$ in about 45 minutes as 'free' molecules (**Ru1**, **Ru2** and $Ru(phen)_3Cl_2$) did in 6–7 min. A semi-quantitative estimation of the relative rate constants for the DHN photooxidation processes (k_{obs}) was accomplished by applying the steady-state approximation to the $^1O_2$ intermediate species, as described in detail in the ESI†; the obtained results are listed in Table 1. The slightly lower efficiency in the $^1O_2$ production found for protein-embedded ruthenium complexes if compared to ones of non-encapsulated molecules is a common feature that has been also observed for other PS agents confined into apoferritin[22] or linked to polymeric structures.[44]

We can rationalize this behavior by considering the fact that quenching of excited triplet states of sensitizers by $^3O_2$ requires the interaction of the PS and molecular oxygen. In this view, while $^3O_2$ can easily diffuse inside ferritin, the mobility of the PS molecules embedded into HuHf would be significantly reduced relative to non-encapsulated metal complexes, due to their interaction with the protein surface (Fig. 2b, c and ESI, Fig. S5b†).

The effectiveness of metal-protein composites in the $^1O_2$ production has been then confirmed from an independent experiment, by monitoring the green fluorescence emission (at 525 nm) of the commercially available Singlet Oxygen Sensor Green® reagent (SOSGR), a highly selective probe for $^1O_2$.[46,47] As shown in Fig. 3b, the irradiation over a period of time of solutions containing the probe in the presence of **Ru1**@HuHf or **Ru2**@HuHf determined a progressive increase of the SOSGR fluorescence emission, revealing a similar ability of Ru(II)-HuHf systems to sensitize $^1O_2$ generation, even though inferior to that of free molecules in agreement with the UV-visible analysis. Of note, the linear increase of the SOSGR luminescence observed for the first irradiation intervals suggests a prompt reaction between the encapsulated PSs and molecular oxygen, thus highlighting the facile diffusion of O_2 into ferritin, a key factor in the iron(II) oxidation reaction occurring in ferritin nanocages. During the same time frame, modest signal changes were observed upon irradiation of a control containing only the probe, or for a solution containing the probe and $[Ru(phen)_3]^{2+}$ held in dark conditions.

TfR1 targeting ability of ruthenium-ferritin assemblies

The targeting ability of cell models expressing TfR1 and the delivery of **Ru1**@HuHf and **Ru2**@HuHf into the cytosol were tested by different biological approaches.

Due to the binding of H-ferritin to TfR1,[9] we evaluated the cellular drug delivery of ruthenium-HuHf nanocomposites in cell lines featuring different expression levels of TfR1. The expression of TfR1 was first analyzed in cervical carcinoma (HeLa) and ovarian carcinoma (A2780) cells, both human cancer cell lines, and in C2C12 myoblasts, a non-tumoral cell line, by western blot analysis in different culture conditions. As shown in Fig. 4, the TfR1 protein level was appreciable in HeLa and A2780 cells, its expression being higher under growth compared to serum-deprivation conditions, whereas it was undetectable in non-cancer C2C12 myoblasts. The expression and localization of TfR1 in these cellular models were further confirmed by confocal immunofluorescence analysis (ESI, Fig. S12†). Subsequently, the uptake of Ru-ferritin nanocomposites in different cellular models was assessed by measuring the content of ruthenium in cell lysates by ICP analysis (Fig. 5a). As shown in Fig. 5a, HeLa and A2780 cells were found to be both able to internalize **Ru1**@HuHf and **Ru2**@HuHf, with no significant differences among the two PS-ferritin formulations. Conversely, lysates of C2C12 myoblasts did not contain detectable amounts of ruthenium, as expected due to the lack of TfR1 expression emerged from western blot (Fig. 4).

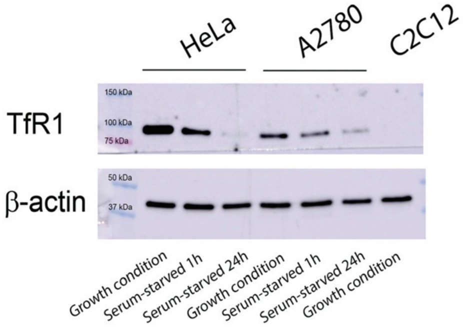

Fig. 4 Expression of TfR1 in cancer (HeLa and A2780) and non-cancer (C2C12) cell lines under different culture conditions. Western blot analysis was performed starting from 20 μg total protein lysates of cells incubated in 10% FBS supplemented growth medium (growth conditions), or serum-deprived medium supplemented with 0.1% BSA for 1 h and 24 h (serum-starved 1 h or 24 h) using specific mouse, monoclonal anti-TfR1 antibody CD71, OKT-9 (Thermo Fisher Scientific). Beta-actin (β-Actin) expression was evaluated as a loading control in each sample using specific antibodies. A blot representative of three independent experiments is shown.

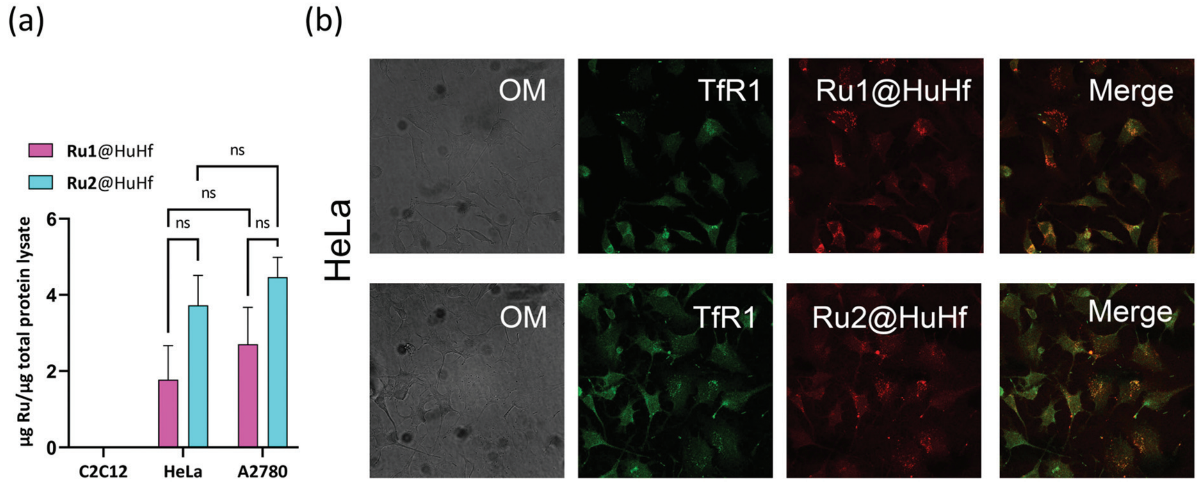

Fig. 5 Cell internalization of **Ru1**@HuHf and **Ru2**@HuHf. (a) The amount of internalized ruthenium after 24 h of incubation of Ru-ferritin nanocomposites (10 µM of encapsulated ruthenium) for each cell line is reported. The ruthenium content in C2C12 cells was not detectable indicating that ferritin is not endocytosed by this cell line. ICP data were normalized on the µg of total protein of each specimen. Statistical analysis was performed by 1-way and 2-way ANOVA followed by Bonferroni *post-hoc* test. (b) Laser scanning confocal microscopy on HeLa cells incubated with **Ru1**@HuHf and **Ru2**@HuHf. The concentration of encapsulated ruthenium and the time of incubation are the same as for the ICP analysis. Immunofluorescence analysis was performed using specific anti-TfR1 primary antibody and secondary anti-mouse antibody conjugated with fluorescein (green). Ru(II) nanocages display fluorescence properties, λ_{exc} 440–480 nm and λ_{em} 600–640 nm (red). Representative confocal microscope images show the colocalization of TfR1 with Ru(II) nanocomposites on the right (merge) and the corresponding optical microscope images on the left (OM).

Then, the uptake of Ru(II)-ferritin systems and the possible colocalization with TfR1 in HeLa cells were investigated by exploiting the luminescence properties of Ru(II)-polypyridyl complexes and by immunofluorescence analysis, using specific anti-TfR1 antibodies. Fig. 5b shows the distribution of **Ru1**@HuHf and **Ru2**@HuHf in the intracellular compartment together with TfR1 (merge). The same results were also obtained in A2780 cells (ESI, Fig. S13†).

In vitro cytotoxicity of ruthenium-loaded ferritin systems after photoactivation

To evaluate the light-induced dose-dependent effect of Ru(II)-ferritin assemblies on cancer cell viability, the MTT reduction assay was carried out in HeLa, A2780 and C2C12 cells incubated for 24 h with different concentrations of Ru(II)-HuHf formulations. Photoactivation was applied as described in Experimental section, 24 h before the cell viability was analyzed, while apo HuHf (*i.e.* not loaded with PSs) was used as negative control to subtract any toxicity due to the protein itself. In this regard, apo HuHf did not show significant cellular toxicity in the range of concentrations of 0–10 µM (corresponding to *ca.* 0–40 µM of Ru-PS loaded into ferritin). The obtained results are reported in Fig. 6. As shown in this figure, photosensitization of ferritin-ruthenium nanocomposites markedly affected cell survival of cancer cells, starting from 10 µM Ru(II) for both **Ru1**@HuHf and **Ru2**@HuHf, leading, as an example, to decreased cell viability of approximately 50% at a drug dose of 40 µM of **Ru1**@HuHf. Conversely, a different behavior was exhibited by C2C12 myoblasts, whose cell viability was negligibly influenced by light-activation, as expected due to the lack of **Ru1**@HuHf and **Ru2**@HuHf internalization in the absence of TfR1 expression in these cells. Thus, these results demonstrated the fundamental role played by TfR1 in the cellular uptake, as well as in the phototoxicity, of Ru(II)-HuHf formulations observed in the different cell lines. An analogous dose-dependent MTT analysis was repeated for free **Ru1** and **Ru2**, meaning not encapsulated into ferritin, (ESI, Fig. S14†). Ru-complexes are able to penetrate into the studied cancer cell lines, including the non-cancer C2C12 myoblasts and as expected, they are not completely inert molecules but rather, they are intrinsically toxic. For example, at the maximum dose investigated, **Ru1** and **Ru2** are found to decrease HeLa cell viability by 30 and 15%, respectively. In A2780 and C2C12 cell lines, the cytotoxic effects are even stronger. These data reinforced the importance of two aspects: (i) the targeted delivery to selectively accumulate the photosensitizers at the site of interest and at the same time (ii) the encapsulation into ferritin-based carrier prevents the toxicity exerted by free molecules before photoactivation.

Experimental

Synthesis and materials

All materials were of reagent grade and used without further purification unless otherwise specified.

The synthesis of the polyamino macrocycles **L′** and **L″** are reported in previous works[33,48] while the corresponding ruthenium(II) complexes were prepared according to our previous papers.[31,33]

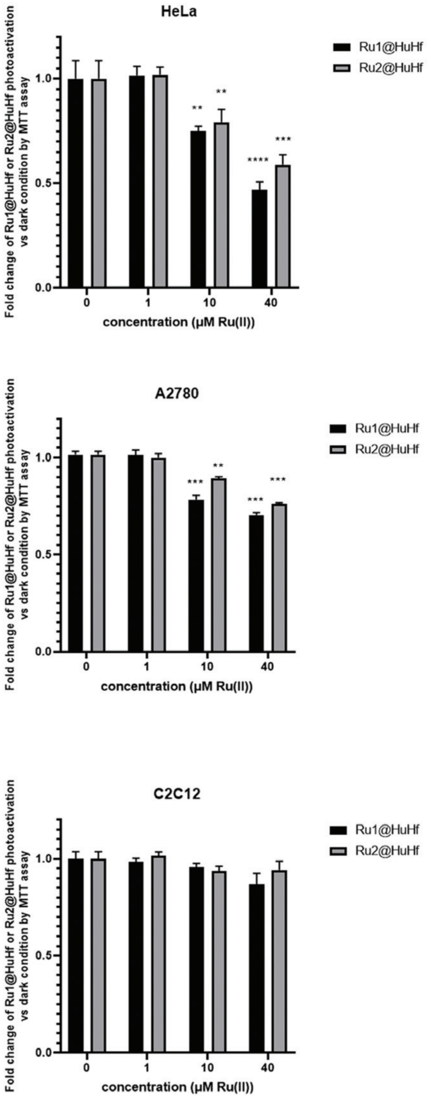

Fig. 6 Dose dependent cytotoxic effect of **Ru1**@HuHf and **Ru2**@HuHf after photoactivation. Cellular viability of different cancer (HeLa and A2780) and non-cancer (C2C12) cell lines was assessed by MTT reduction analysis. Cells were incubated for 24 h in the presence of Ru(II)-HuHf nanocomposites with **Ru1** and **Ru2** at the following concentrations, 0 μm, 1 μM, 10 μM and 40 μM in serum-deprived culture media (supplemented with BSA 0.1%). Photoactivation was carried out using a 30 W three-arm LED lamp with 470–430 nm blue emission for 20 minutes, at a distance of 5 cm from the cell plate. Twenty-four hours after photoactivation, MTT analysis was performed to assess the antitumor effect of Ru(II) nanocages. Experiments were performed in triplicate, representative of three independent ones with similar results. Data reported are mean ± SEM of fold change absorbance at 570 nm in photoactivated compared to dark conditions normalized to apoferritin treatment. The effect of photoactivation of Ru(II) nanocages on the inhibition of cell survival was statistically established by 1-way ANOVA followed by Bonferroni *post-hoc* test. $^{**}P < 0.01$, $^{***}P < 0.001$, $^{****}P < 0.0001$.

Ferritin expression and purification

Homopolymeric human heavy chain ferritin (HuHf) was produced in *E. coli* as previously reported.[42,49,50] The pET-9a plasmid carrying human heavy chain ferritin gene was transformed in BL21(DE3)-pLysS competent cells. Massive cultures were grown in rich Luria-Bertani medium at 37 °C adding kanamycin (50 μg mL^{-1}) and chloramphenicol (34 μg mL^{-1}) antibiotics. The overexpression of the protein was induced at $OD_{600\ nm}$ 0.6–0.8 with 1 mM of isopropyl β-D-1-thiogalactopyranoside (IPTG) for 4 h at 37 °C. At the end, the cells were harvested by centrifugation at 7500 rpm for 15 min and disrupted by sonication. Afterwards, the crude lysate was clarified with ultracentrifugation at 40 000 rpm for 40 min and the supernatant recovered and heated at 65 °C for 15 min to precipitate undesired proteins. The soluble fraction was subjected to anionic exchange chromatography with a linear sodium chloride gradient 0–1 M (Q-Sepharose Fast Flow resin, GE Healthcare) in 20 mM Tris pH 7.5 buffer. Ferritin-containing fractions were identified by SDS-PAGE and then pooled and loaded into a Superdex 200 HiLoad 16/600 column (GE Healthcare) for size exclusion chromatography in 20 mM Tris pH 7.5 buffer. To remove the metal ions taken up from the culture medium, four 5 L dialysis in the presence of chelating and reducing agents (20 mM Tris, 2.5 mM EDTA, 15 mL ammonium thioglycolate pH 7.5 buffer) followed by four dialysis against 5 L of 20 mM Tris pH 7.5 buffer were performed.

Encapsulation of Ru1 and Ru2

Encapsulation of **Ru1** and **Ru2** was promoted by the dissociation of ferritin cage (HuHf in 50 mM sodium phosphate pH 7 buffer) into its monomers at pH 12, diluting the protein solution (final concentration of 1.25 μM HuHf in a final volume of 5 mL) with Universal buffer at pH 12 (Britton Robinson buffer) and adjusting pH adding NaOH 1 M. Different concentrations of **Ru1** or **Ru2** (25, 125 and 250 μM) were incubated with ferritin for 15 min. Then, the pH was brought at 7 with HCl 1 M to let the protein reassemble in a 24-mer cage, trapping **Ru1** and **Ru2** inside the cavity in 2 h. The entire process was run under stirring at 30 °C. At this point, the protein samples were centrifuged at 7000 rpm for 10 min to discard precipitates and extensively filtered in centrifugal devices (Amicon® Ultra 15 mL with cutoff 50 kDa, Merck LifeScience) to remove excess photosensitizers. To recoup the portion of protein with the correct folding, size exclusion chromatography (Superdex 200 10/300 GL column, GE Healthcare) was applied. The encapsulated products were eluted in 50 mM sodium phosphate pH 7 buffer and the fractions with a retention volume corresponding to 24-mer HuHf were recovered. In order to exclude unspecific binding of Ru-based molecules on the external surface of the protein, control experiments with native HuHf were performed incubating **Ru1** and **Ru2** with HuHf in 50 mM sodium phosphate pH 7 buffer avoiding the opening of the protein cage. Protein concentration was determined by Bradford assay. The estimation of ruthenium content was performed by UV-visible and ICP-AES. For the following analysis in cell cultures, the encapsulates were further subjected to buffer exchange in PBS (phosphate buffer solution) at pH 7.4 and 0.2 μm filtered to obtain the sterility required for mammalian cells.

ICP-AES measurements

Samples were treated with 100 μL of suprapure HNO_3 (obtained by sub-boiling distillation) and 100 μL of suprapure HCl (30%) and, after dissolution, were diluted to a final volume of 5.0 mL with ultrapure water (UHQ – resistivity >18 MΩ cm – Milli-Q system by Millipore, Billerica, MA). The determination of Ru concentrations in the samples was performed in triplicate by a Varian 720-ES axial inductively coupled plasma atomic emission spectrometer (ICP-AES). Each sample was spiked with 1.0 ppm of Ge used as an internal standard prior to the analysis. The introduction system consisted of a concentric pneumatic nebulizer and a cyclonic spray chamber. Calibration standards were prepared by gravimetric serial dilution from commercial stock standard solutions of Ru at 1000 mg L^{-1} (Honeywell Fluka). Wavelengths used for Ru determination were 267.876 and 245.657 nm, whereas for Ge the line at 209.426 nm was used. The operating conditions were optimized to obtain maximum signal intensity, and between each sample, a rinsing solution constituted by 2% v/v of HNO_3 was used.

UV-visible, fluorescence and circular dichroism analysis

Absorption spectra were registered on a PerkinElmer Lambda 6 spectrophotometer. The electronic absorption profiles of **Ru1**@HuHf and **Ru2**@HuHf were compared with the spectra of the reference compounds **Ru1** and **Ru2**. All the spectra were registered in 50 mM sodium phosphate pH 7 buffer. The quantity of the compounds internalized into HuHf was initially calculated with the absorbance at 450 nm of Ru(II)-centers given the extinction molar coefficients of **Ru1** and **Ru2**. In order to evaluate the luminescence of **Ru1** and **Ru2** upon encapsulation, the fluorescence of 6 μM free and encapsulated **Ru1** and **Ru2** was read using excitation and emission wavelengths of 411 nm and 615 nm respectively. In addition, the intrinsic fluorescence of HuHf (0.3 μM in protein cage) was registered at 325 nm upon excitation of tryptophan and tyrosine aromatic residues at 280 nm for apo HuHf and for HuHf loaded with increasing amounts of **Ru1** (0.7 μM, 2.01 μM and 2.60 μM) and **Ru2** (0.58 μM, 1.77 μM and 1.85 μM). Fluorescence measurements were collected on a PerkinElmer LS55 spectrofluorometer. The slit width set for excitation and emission was 10 nm. All measurements were performed at 298.0 ± 0.1 K in 50 mM sodium phosphate buffer solution pH 7, while spectra at different pH values were collected by adding small amounts of concentrated HCl or NaOH to aqueous solutions of ligands.

Circular dichroism (CD) analysis was conducted with a Jasco spectropolarimeter J-810 in the far-UV region between 190–250 nm with a 0.1 cm path length quartz cuvette. Temperature-dependent CD spectra of 10 μM protein in subunits (50 mM sodium phosphate pH 7) were performed in the range 25–85 °C. The samples were incubated in the thermostatic cell (Jasco Peltier equipment) at the desired temperatures for 5 min before acquiring spectra at a scanning speed of 100 nm min^{-1}. The mean of 5 scans was calculated by subtracting the corresponding buffer spectrum and the molar ellipticity optical units were converted in mean residue weight ellipticity (θ_{MRW}).

SAXS measurements

All small-angle scattering measurements were performed using a HECUS S3-Micro apparatus. This Kratky-type camera is equipped with a position sensitive, 50 M OED detector comprising of 1024 channels (width = 54 μm). Cu Kα radiation with a wavelength, λ, of 1.542 Å at a power of 50 W is provided by an ultra-brilliant point microfocus X-ray generator (GENIX-Fox 3D, Xenocs, Grenoble). A sample-to-detector distance of 281 mm (calibrated using the well-known silver behenate lamellar lattice, d = 58.34 Å[16] provided a measurable q-range between 0.009 and 0.54 $Å^{-1}$ (where q, the scattering vector, is given by $q = 4\pi/\lambda \sin\theta$, and 2θ is the scattering angle). Protein samples were placed into borosilicate glass capillaries with a diameter of 1 mm. Measurements were performed under vacuum to reduce scattering from air and at a temperature of 25 °C. Raw scattering data were corrected for the empty capillary/buffer contribution. The acquisition time was from 30 min to 1 h depending on the sample. Short measurements (1 min) were performed on each sample to confirm that the radiation damage was negligible under these experimental conditions.

^{1}H NMR analysis

^{1}H NMR spectra of free **Ru1** and **Ru2** (100 μM), apo HuHf (25 μM in cage) and **Ru1**@HuHf and **Ru2**@HuHf (100 μM of encapsulated **Ru1**/**Ru2**) in phosphate NMR buffer (pH 7.4) were recorded and compared to further investigate the interaction of the encapsulated Ru-compounds with HuHf. NMR spectra were acquired using a Bruker 900 MHz spectrometer (Bruker BioSpin) at 298 K. One-dimensional ^{1}H-NMR spectra with water peak suppression and a standard CPMG pulse sequence were recorded (3k scans, 102 400 data points, a spectral width of 19 167 Hz, acquisition time of 2.97 s, and a relaxation delay of 4 s).[40,41] This type of sequence has been used to selectively observe the sharp signals arising from the low molecular weight Ru-compounds free in solution and to suppress the broad resonances coming from ferritin. Before applying Fourier transform, free induction decays were multiplied by an exponential function equivalent to a 2.0 Hz line-broadening factor. Transformed spectra were automatically corrected for phase and baseline distortions using TopSpin 3.5 (Bruker BioSpin). The spectra of free **Ru1** and **Ru2** were also recorded in plasma to prove their long-term stability in biological fluids (ESI, Fig. S1†).

Zeta potential measurements

Zeta potential measurements were performed with a ZetaPALS system coupled with a Brookhaven 90Plus particle sizer (Brookhaven Instruments). Measurements were performed on the very same dispersions and also after dilution up to 1 : 20 to reduce the overall ionic strength. Zeta potentials of the scattering objects were extracted by phase analysis light scattering according to standard procedures.

Cryo-EM screening analysis

Cryo-EM micrographs of apo HuHf, **Ru1**@HuHf and **Ru2**@HuHf were acquired using a ThermoFisher Glacios at 200 kV instrument, equipped with a Falcon III direction electron detector. Holey-carbon R1.2/1.3 grids (Quantifoil Micro Tools GmbH) covered by a 2 nm film of carbon were prepared. Grid surfaces were treated with plasma cleaning using O2 for 45 s before applying 3 μL of the sample (1 mg mL^{-1} of **Ru1**@HuHf and **Ru2**@HuHf in PBS buffer pH 7.4). Grids were blotted in 100% humidity and 10 °C with filter paper and vitrified by rapidly plunging into liquid ethane at −180 °C using a Vitrobot Mark IV (FEI, Hillsboro).

Singlet oxygen determination using 1,5-dihydroxynaphthalene (DHN) and the singlet oxygen sensor green reagent (SOSGR)

The ability of Ru-based formulations to effectively sensitize the singlet oxygen production was firstly assessed by means of UV visible titrations employing 1,5-dihydroxynaphthalene (DHN) as an indirect $^1O_2$ reporter. Experiments were performed in phosphate buffer (50 mM, pH 7, with 10% v/v MeOH and D_2O each)[44] in the absence and in the presence of a selected Ru(II)-based photosensitizer. In detail, following the preparation of a 3.3×10^{-3} M solution of DHN in methanol, this solution was diluted 1 : 10 with aqueous solutions of the Ru(II)-based PS at pH 7, obtaining a final water/MeOH (9 : 1) solution of DHN 3.3×10^{-4} M with a Ru(II)-content of 1×10^{-5} M. Samples were then transferred in a quartz cuvette with 1 cm optical path and irradiated (LED Lamp, 30 W, $\lambda > 430$ nm) for a total time varying between 6 and 50 minutes. All spectra were acquired using as blank reference a solution containing the selected PS at the same concentration and pH of those of the measuring cuvette. In close analogy with the UV-vis measurements, the $^1O_2$ sensitizing properties of the studied formulations were investigated by means of fluorescence measurements by employing the Singlet Oxygen Sensor Green reagent (SOSGR).[46] To this aim, we prepared aqueous solutions buffered at pH 7 (50 mM sodium phosphate) containing SOSGR in the presence of a selected photosensitizer. The probe concentration was fixed to 0.5 μM while the ruthenium concentrations of **Ru1** and **Ru2** were ten times higher (5 μM). Samples containing **Ru1**@HuHf or **Ru2**@HuHf were prepared in order to have a final Ru(II) equivalent concentration. The solutions were then transferred in a quartz cuvette with 0.1 cm optical path and irradiated. Fluorescence spectra were collected using excitation/emission wavelengths of 488/525 nm. Two additional controls were analyzed, one containing a mixture of SOSGR and $[Ru(phen)_3]^{2+}$ maintained under dark conditions, and the other consisting of only the probe exposed to different irradiation times.

Cell cultures

All culture media and reagents were purchased from Merck KGaA (Darmstadt, Germany), including phosphate buffer saline (PBS). Human ovarian cancer cell line A2780 and human epithelioid cervix carcinoma cell line HeLa (ATCC, VA, USA) were cultured in RPMI-1640 medium supplemented with 10% fetal bovine serum (FBS), 100 μg mL^{-1} streptomycin, 100 U mL^{-1} penicillin and 2 mM l-glutamine. C2C12 myoblasts (ATCC, VA, USA) were cultured in Dulbecco's Modified Eagle's Medium (DMEM) supplemented with 10% FBS, 100 μg mL^{-1} streptomycin, 100 U mL^{-1} penicillin and 2 mM l-glutamine. These cell lines were maintained in a humidified atmosphere at 95% air/55% CO_2 and constant temperature of 37 °C.

All cell treatments were performed in serum-deprived RPMI or DMEM medium, supplemented with 1 mg mL^{-1} bovine serum albumin (0.1% BSA).

Western blot analysis

Cells were collected in a lysis buffer containing 50 mM Tris, pH 7.5, 120 mM NaCl, 1 mM EDTA, 6 mM EGTA, 15 mM $Na_4P_2O_7$, 20 mM NaF, and 1% Nonidet supplemented with protease inhibitor cocktail and incubated 30 min at 4 °C. Cell lysates were centrifuged at 10^4g, 15 min 4 °C and 20 μg total protein amount was resuspended in sodium dodecyl sulphate (SDS) sample buffer and separated by SDS-polyacrylamide gel electrophoresis (SDS-PAGE) and finally transferred to polyvinylidene fluoride (PVDF) membranes by Trans-Blot® turbo transfer system (Bio-Rad Laboratories, CA, USA). PVDF membranes were incubated at 4 °C overnight with anti-CD71 (Transferrin receptor-1) monoclonal antibody (OKT-9; 1 : 1000 dilution) (eBioscience, Thermo Fisher Scientific Inc., MA, USA) and anti-β-actin (Santa Cruz Biotechnology, CA, USA). Horseradish peroxidase (HRP)-conjugated secondary antibodies (Santa Cruz Biotechnology, CA, USA) were incubated for 1 h at room temperature. Specific protein bands were detected by enhanced chemiluminescence using Clarity Western ECL substrate (Bio-Rad Laboratories, CA, USA), images were acquired with an Amersham Imager 600 (GE Healthcare, UK) and quantification performed by densitometric analysis using the ImageJ software (freely available at https://imagej.nih.gov/ij/).

MTT reduction assay

Cell viability of HeLa, A2780 and C2C12 cells was evaluated by the reduction of the yellow tetrazolium salt 3-(4,5-dimethylthiazol-2-yl)-2,5-diphenyltetrazolium bromide (MTT) to purple formazan crystals performed by metabolically active cells. MTT colorimetric analysis was performed after the treatment with **Ru1**@HuHf or **Ru2**@HuHf for 24 h, followed by photoactivation and then incubation for further 24 h. Briefly, for each cell line two 96-well plates were seeded: one was employed for light exposure (photoactivation conditions), and the other one was maintained in the dark (dark conditions). Cells were incubated with increasing concentrations of Ru(II) in **Ru1**@HuHf or **Ru2**@HuHf obtained by ICP measurement (0, 1, 10 and 40 μM), and in parallel with the same corresponding concentration of HuHf (determined by Bradford assay) in serum-deprived culture media. For the photoactivation conditions, after a 24 h-challenge with Ru(II) nanocages, cells were irradiated with 30 W three-arm LED light lamp with 470 nm–430 nm emission for 20 minutes at a distance of 5 cm from cell monolayers and then incubated for 24 h at 37 °C in 5% CO_2 atmosphere. Cell viability was assayed in the presence of 0.5 mg mL^{-1} of MTT salt (Merck KGaA, Darmstadt, Germany) for 1 h at 37 °C; DMSO (Dimethyl Sulfoxide, Merck KGaA, Darmstadt, Germany) was used to dissolve insoluble formazan crystals produced by viable cells. The absorbance was measured at 595 nm using a microplate reader (iMark Microplate Absorbance Reader, Bio-Rad, CA, USA).

Laser scanning confocal microscopy

Cell internalization of ferritin-Ru(II) nanocages and colocalization analysis with transferrin receptor-1 was performed using a Leica SP8 laser scanning confocal microscope (Leica Microsystems GmbH). Cells (HeLa, A2780 and C2C12) were seeded on microscope slides and treated for 24 h with 10 μM Ru(II) of **Ru1**@HuHf or **Ru2**@HuHf, followed by washing with PBS and fixed with 2% paraformaldehyde in PBS for 20 minutes at room temperature. Colocalization of **Ru1**@HuHf or **Ru2**@HuHf with anti-CD71 (transferrin receptor-1) was performed by immunofluorescence analysis: after 24 h of incubation with 10 μM Ru(II) of **Ru1**@HuHf or **Ru2**@HuHf, microscope slides were incubated with anti-CD71 (TfR1) monoclonal antibody (OKT-9; 1 : 100 dilution) for 2 h at room temperature followed by treatment with Texas Red-conjugate secondary anti-rabbit antibody (1 : 200 dilution) purchased from Vector Laboratories Inc. (Burlingame, CA, USA). Microscope slides were incubated with DAPI solution (1 mg ml^{-1}, Thermo Fisher Scientific Inc., MA, USA) to probe the cell nucleus and then were mounted using Fluoromount aqueous mounting medium (Merck KGaA, Darmstadt, Germany).

Statistical analysis

Data obtained in the cell experiments are presented as means ± standard error of mean (SEM). Comparisons between the different groups were performed by one- or two-way ANOVA analysis of variances followed by Bonferroni's *post-hoc* test in the GraphPad Prism 9.0 software.

Conclusions

In summary, we herein report on the successful encapsulation into human H-ferritin of the photosensitizers **Ru1** and **Ru2**, affording the corresponding **Ru1**@HuHf and **Ru2**@HuHf nanocomposites.

A chemical–physical characterization of these fluorescent hybrid materials evidenced a retained protein quaternary structure (*i.e.* core–shell assembly and protein fold), with **Ru1** and **Ru2** giving rise to intermolecular contacts/interactions with the inner surface of the protein shell. Importantly, Ru(II)-ferritin assemblies featured high stability at physiological pH and demonstrated to effectively sensitize $^1O_2$ production upon light-activation.

The biological potential of **Ru1**@HuHf and **Ru2**@HuHf was tested against two human cancer cell lines, HeLa and A2780 cells, both expressing TfR1, and on the non-tumoral C2C12 myoblasts. ICP analysis indicated the selective internalization of Ru(II)-HuHf assemblies into tumoral cells. Confocal microscopy analysis also unveiled the co-localization of **Ru1** and **Ru2** with the TfR1 in the internal cellular compartments of HeLa and A2780 cells. Therefore, these results highlighted the crucial role played by TfR1-mediated endocytosis of H-type ferritin in the selective delivery of Ru-based PSs into tumoral cells.

Finally, **Ru1**@HuHf and **Ru2**@HuHf were found to be effectively able to elicit a significant dose-dependent cytotoxicity against HeLa and A2780 cells following irradiation.

In conclusion, this study underlines the suitability of H-ferritin platforms to selectively deliver Ru(II)-polypyridyl-based photosensitizers in cancer cells thus providing promising tools to be further exploited in photodynamic therapy.

Author contributions

L. Con. and G. E. G. synthesized the Ru(II) compounds. S. C. and L. Con. produced ferritin and its nanocomposites. L. Con. and S. C. carried out spectrophotometric characterization and measured singlet oxygen production. V. G., M. S. and E. F. performed ^1H NMR, ICP-AES and SAXS experiments, respectively. E. P., F. C. and P. B. conducted cell experiments. L. Con. and S. C. wrote the manuscript. P. B. and B. V. revised the manuscript. P. T. conceived the study and provided funding. C. G. and P. T. supervised the work.

Conflicts of interest

There are no conflicts to declare.

Acknowledgements

The authors thank Dr Giovanni Ferraro for zeta-potential measurements. Fondazione Cassa di Risparmio di Firenze funded the project "Development of ferritin-based nanodevices for the targeted delivery of drugs and imaging probes", which includes a research grant to L. Cos. The authors acknowledge MIUR for "Progetto Dipartimenti di Eccellenza 2018–2022" allocated to the Department of Chemistry "Ugo Schiff" and to the Department of Experimental and Clinical Biomedical Sciences "Mario Serio". E. F. acknowledges the financial support from CSGI. S. C. was supported by an AIRC fellowship for Italy. We acknowledge Instruct-ERIC, a Landmark ESFRI project, for the support and the use of resources and specifically the CERM/CIRMMP Italy Centre. The authors thank FloCEN, the Florence Centre for Electron Nanoscopy of the Department of Chemistry "Ugo Schiff", University of Florence, for Cryo-EM screening analysis.

Notes and references

1 R. R. Crichton, Structure and function of ferritin, *Angew. Chem., Int. Ed. Engl.*, 1973, **12**, 57–65.

2 S. Ciambellotti, C. Pozzi, S. Mangani and P. Turano, Iron Biomineral Growth from the Initial Nucleation Seed in L-Ferritin, *Chem. – Eur. J.*, 2020, **26**, 5770–5773.

3 C. Pozzi, S. Ciambellotti, C. Bernacchioni, F. Di Pisa, S. Mangani and P. Turano, Chemistry at the protein-mineral interface in L-ferritin assists the assembly of a functional (μ3-oxo)Tris[(μ2-peroxo)] triiron(III) cluster, *Proc. Natl. Acad. Sci. U. S. A.*, 2017, **114**, 2580–2585.

4 J. D. López-Castro, J. J. Delgado, J. A. Perez-Omil, N. Gálvez, R. Cuesta, R. K. Watt and J. M. Domínguez-Vera, A new approach to the ferritin iron core growth: influence of the H/L ratio on the core shape, *Dalton Trans.*, 2012, **41**, 1320–1324.

5 C. Quintana, J. M. Cowley and C. Marhic, Electron nanodiffraction and high-resolution electron microscopy studies of the structure and composition of physiological and pathological ferritin, *J. Struct. Biol.*, 2004, **147**, 166–178.

6 N. Gálvez, B. Fernández, P. Sánchez, R. Cuesta, M. Ceolín, M. Clemente-León, S. Trasobares, M. López-Haro, J. J. Calvino, O. Stéphan and J. M. Domínguez-Vera, Comparative Structural and Chemical Studies of Ferritin Cores with Gradual Removal of their Iron Contents, *J. Am. Chem. Soc.*, 2008, **130**, 8062–8068.

7 P. Arosio, F. Carmona, R. Gozzelino, F. Maccarinelli and M. Poli, The importance of eukaryotic ferritins in iron handling and cytoprotection, *Biochem. J.*, 2015, **472**, 1–15.

8 G. Jutz, P. van Rijn, B. Santos Miranda and A. Böker, Ferritin: a versatile building block for bionanotechnology, *Chem. Rev.*, 2015, **115**, 1653–1701.

9 L. Li, C. J. Fang, J. C. Ryan, E. C. Niemi, J. A. Lebrón, P. J. Björkman, H. Arase, F. M. Torti, S. V. Torti, M. C. Nakamura and W. E. Seaman, Binding and uptake of H-ferritin are mediated by human transferrin receptor-1, *Proc. Natl. Acad. Sci. U. S. A.*, 2010, **107**, 3505–3510.

10 L. C. Montemiglio, C. Testi, P. Ceci, E. Falvo, M. Pitea, C. Savino, A. Arcovito, G. Peruzzi, P. Baiocco, F. Mancia, A. Boffi, A. des Georges and B. Vallone, Cryo-EM structure of the human ferritin-transferrin receptor 1 complex, *Nat. Commun.*, 2019, **10**, 1121.

11 M. Truffi, L. Fiandra, L. Sorrentino, M. Monieri, F. Corsi and S. Mazzucchelli, Ferritin nanocages: A biological platform for drug delivery, imaging and theranostics in cancer, *Pharmacol. Res.*, 2016, **107**, 57–65.

12 G. Ferraro, S. Ciambellotti, L. Messori and A. Merlino, Cisplatin Binding Sites in Human H-Chain Ferritin, *Inorg. Chem.*, 2017, **56**, 9064–9070.

13 G. Fracasso, E. Falvo, G. Colotti, F. Fazi, T. Ingegnere, A. Amalfitano, G. B. Doglietto, S. Alfieri, A. Boffi, V. Morea, G. Conti, E. Tremante, P. Giacomini, A. Arcovito and P. Ceci, Selective delivery of doxorubicin by novel stimuli-sensitive nano-ferritins overcomes tumor refractoriness, *J. Controlled Release*, 2016, **239**, 10–18.

14 E. Falvo, E. Tremante, R. Fraioli, C. Leonetti, C. Zamparelli, A. Boffi, V. Morea, P. Ceci and P. Giacomini, Antibody-drug conjugates: targeting melanoma with cisplatin encapsulated in protein-cage nanoparticles based on human ferritin, *Nanoscale*, 2013, **5**, 12278–12285.

15 W. Liu, Q. Lin, Y. Fu, S. Huang, C. Guo, L. Li, L. Wang, Z. Zhang and L. Zhang, Target delivering paclitaxel by ferritin heavy chain nanocages for glioma treatment, *J. Controlled Release*, 2019, **323**, 191–202.

16 S. Ciambellotti, A. Pratesi, M. Severi, G. Ferraro, E. Alessio, A. Merlino and L. Messori, The NAMI A - human ferritin system: a biophysical characterization, *Dalton Trans.*, 2018, **47**, 11429–11437.

17 J. C. Cutrin, D. Alberti, C. Bernacchioni, S. Ciambellotti, P. Turano, C. Luchinat, S. G. Crich and S. Aime, Cancer cell death induced by ferritins and the peculiar role of their labile iron pool, *Oncotarget*, 2018, **9**, 27974–27984.

18 D. E. J. G. J. Dolmans, D. Fukumura and R. K. Jain, Photodynamic therapy for cancer, *Nat. Rev. Cancer*, 2003, **3**, 380–387.

19 P.-C. Lo, M. S. Rodríguez-Morgade, R. K. Pandey, D. K. P. Ng, T. Torres and F. Dumoulin, The unique features and promises of phthalocyanines as advanced photosensitisers for photodynamic therapy of cancer, *Chem. Soc. Rev.*, 2020, **49**, 1041–1056.

20 G. Boccalini, L. Conti, C. Montis, D. Bani, A. Bencini, D. Berti, C. Giorgi, A. Mengoni and B. Valtancoli, Methylene blue-containing liposomes as new photodynamic anti-bacterial agents, *J. Mater. Chem. B*, 2017, **5**, 2788–2797.

21 Z. Zhen, W. Tang, C. Guo, H. Chen, X. Lin, G. Liu, B. Fei, X. Chen, B. Xu and J. Xie, Ferritin nanocages to encapsulate and deliver photosensitizers for efficient photodynamic therapy against cancer, *ACS Nano*, 2013, **7**, 6988–6996.

22 F. Yan, Y. Zhang, H. Yuan, M. K. Gregas and T. Vo-Dinh, Apoferritin protein cages: a novel drug nanocarrier for photodynamic therapy, *Chem. Commun.*, 2008, 4579–4581.

23 L. Li, S. Zhou, N. Lv, Z. Zhen, T. Liu, S. Gao, J. Xie and Q. Ma, Photosensitizer-Encapsulated Ferritins Mediate Photodynamic Therapy against Cancer-Associated Fibroblasts and Improve Tumor Accumulation of Nanoparticles, *Mol. Pharm.*, 2018, **15**, 3595–3599.

24 Z. Zhen, W. Tang, W. Zhang and J. Xie, Folic acid conjugated ferritins as photosensitizer carriers for photodynamic therapy, *Nanoscale*, 2015, **7**, 10330–10333.

25 M. Liu, Y. Zhu, T. Wu, J. Cheng and Y. Liu, Nanobody-Ferritin Conjugate for Targeted Photodynamic Therapy, *Chemistry*, 2020, **26**, 7442–7450.

26 C. Mari, V. Pierroz, R. Rubbiani, M. Patra, J. Hess, B. Spingler, L. Oehninger, J. Schur, I. Ott, L. Salassa, S. Ferrari and G. Gasser, DNA intercalating Ru(II) polypyridyl complexes as effective photosensitizers in photodynamic therapy, *Chemistry*, 2014, **20**, 14421–14436.

27 S. Monro, K. L. Colón, H. Yin, J. Roque, P. Konda, S. Gujar, R. P. Thummel, L. Lilge, C. G. Cameron and S. A. McFarland, Transition Metal Complexes and

Photodynamic Therapy from a Tumor-Centered Approach: Challenges, Opportunities, and Highlights from the Development of TLD1433, *Chem. Rev.*, 2019, **119**, 797–828.

28 G. E. Giacomazzo, L. Conti, A. Guerri, M. Pagliai, C. Fagorzi, P. S. Sfragano, I. Palchetti, G. Pietraperzia, A. Mengoni, B. Valtancoli and C. Giorgi, Nitroimidazole-Based Ruthenium(II) Complexes: Playing with Structural Parameters to Design Photostable and Light-Responsive Antibacterial Agents, *Inorg. Chem.*, 2021, DOI: 10.1021/acs.inorgchem.1c03032.

29 D. M. Monti, G. Ferraro and A. Merlino, Ferritin-based anticancer metallodrug delivery: Crystallographic, analytical and cytotoxicity studies, *Nanomedicine*, 2019, **20**, 101997.

30 X. Li, Y. Zhang, H. Chen, J. Sun and F. Feng, Protein Nanocages for Delivery and Release of Luminescent Ruthenium(II) Polypyridyl Complexes, *ACS Appl. Mater. Interfaces*, 2016, **8**, 22756–22761.

31 L. Conti, A. Bencini, C. Ferrante, C. Gellini, P. Paoli, M. Parri, G. Pietraperzia, B. Valtancoli and C. Giorgi, Highly Charged Ruthenium(II) Polypyridyl Complexes as Effective Photosensitizer in Photodynamic Therapy, *Chemistry*, 2019, **25**, 10606–10615.

32 L. Conti, A. Mengoni, G. E. Giacomazzo, L. Mari, M. Perfetti, C. Fagorzi, L. Sorace, B. Valtancoli and C. Giorgi, Exploring the potential of highly charged Ru(II)- and heteronuclear Ru(II)/Cu(II)-polypyridyl complexes as antimicrobial agents, *J. Inorg. Biochem.*, 2021, **220**, 111467.

33 L. Conti, L. Mummolo, G. M. Romano, C. Giorgi, G. E. Giacomazzo, L. Prodi and A. Bencini, Exploring the Ability of Luminescent Metal Assemblies to Bind and Sense Anionic or Ionizable Analytes A Ru(phen)2bipy-Based Dizinc Complex for Bisphenol A (BPA) Recognition, *Molecules*, 2021, **26**, 527.

34 J. Zhang, D. Cheng, J. He, J. Hong, C. Yuan and M. Liang, Cargo loading within ferritin nanocages in preparation for tumor-targeted delivery, *Nat. Protoc.*, 2021, **16**, 4878–4896.

35 R. R. Crichton and C. F. A. Bryce, Subunit interactions in horse spleen apoferritin. Dissociation by extremes of pH, *Biochem. J.*, 1973, **133**, 289–299.

36 C. T. Lin, W. Boettcher, M. Chou, C. Creutz and N. Sutin, Mechanism of the quenching of the emission of substituted polypyridineruthenium(II) complexes by iron(III), chromium(III), and europium(III) ions, *J. Am. Chem. Soc.*, 1976, **98**, 6536–6544.

37 G. Petruk, D. M. Monti, G. Ferraro, A. Pica, L. D'Elia, F. Pane, A. Amoresano, J. Furrer, K. Kowalski and A. Merlino, Encapsulation of the Dinuclear Trithiolato-Bridged Arene Ruthenium Complex Diruthenium-1 in an Apoferritin Nanocage: Structure and Cytotoxicity, *ChemMedChem*, 2019, **14**, 594–602.

38 S. Stefanini, E. Chiancone and E. Antonini, Iron binding to apoferritin: a fluorescence spectroscopy study, *FEBS Lett.*, 1976, **69**, 90–94.

39 J. Michon, S. Frelon, C. Garnier and F. Coppin, Determinations of uranium(VI) binding properties with some metalloproteins (transferrin, albumin, metallothionein and ferritin) by fluorescence quenching, *J. Fluoresc.*, 2010, **20**, 581–590.

40 A. Vignoli, V. Ghini, G. Meoni, C. Licari, P. G. Takis, L. Tenori, P. Turano and C. Luchinat, High-Throughput Metabolomics by 1D NMR, *Angew. Chem., Int. Ed.*, 2019, **58**, 968–994.

41 P. G. Takis, V. Ghini, L. Tenori, P. Turano and C. Luchinat, Uniqueness of the NMR approach to metabolomics, *TrAC, Trends Anal. Chem.*, 2019, **120**, 115300.

42 C. Pozzi, F. Di Pisa, C. Bernacchioni, S. Ciambellotti, P. Turano and S. Mangani, Iron binding to human heavy-chain ferritin, *Acta Crystallogr., Sect. D: Biol. Crystallogr.*, 2015, **71**, 1909–1920.

43 A. A. Abdel-Shafi, M. D. Ward and R. Schmidt, Mechanism of quenching by oxygen of the excited states of ruthenium (II) complexes in aqueous media. Solvent isotope effect and photosensitized generation of singlet oxygen, O2(1Deltag), by [Ru(diimine)(CN)4]2- complex ions, *Dalton Trans.*, 2007, 2517–2527.

44 D. Maggioni, M. Galli, L. D'Alfonso, D. Inverso, M. V. Dozzi, L. Sironi, M. Iannacone, M. Collini, P. Ferruti, E. Ranucci and G. D'Alfonso, A luminescent poly(amidoamine)-iridium complex as a new singlet-oxygen sensitizer for photodynamic therapy, *Inorg. Chem.*, 2015, **54**, 544–553.

45 S. Takizawa, R. Aboshi and S. Murata, Photooxidation of 1,5-dihydroxynaphthalene with iridium complexes as singlet oxygen sensitizers, *Photochem. Photobiol. Sci.*, 2011, **10**, 895–903.

46 A. Gollmer, J. Arnbjerg, F. H. Blaikie, B. W. Pedersen, T. Breitenbach, K. Daasbjerg, M. Glasius and P. R. Ogilby, Singlet Oxygen Sensor Green®: photochemical behavior in solution and in a mammalian cell, *Photochem. Photobiol.*, 2011, **87**, 671–679.

47 T. Entradas, S. Waldron and M. Volk, The detection sensitivity of commonly used singlet oxygen probes in aqueous environments, *J. Photochem. Photobiol., B*, 2020, **204**, 111787.

48 C. Lodeiro, A. J. Parola, F. Pina, C. Bazzicalupi, A. Bencini, A. Bianchi, C. Giorgi, A. Masotti and B. Valtancoli, Protonation and Zn(II) coordination by dipyridine-containing macrocycles with different molecular architecture. A case of pH-controlled metal jumping outside-inside the macrocyclic cavity, *Inorg. Chem.*, 2001, **40**, 2968–2975.

49 E. Ravera, S. Ciambellotti, L. Cerofolini, T. Martelli, T. Kozyreva, C. Bernacchioni, S. Giuntini, M. Fragai, P. Turano and C. Luchinat, Solid-State NMR of PEGylated Proteins, *Angew. Chem., Int. Ed.*, 2016, **55**, 2446–2449.

50 S. Zanzoni, K. Pagano, M. D'Onofrio, M. Assfalg, S. Ciambellotti, C. Bernacchioni, P. Turano, S. Aime, L. Ragona and H. Molinari, Unsaturated Long-Chain Fatty Acids Are Preferred Ferritin Ligands That Enhance Iron Biomineralization, *Chemistry*, 2017, **23**, 9879–9887.